Article

Metastable nickel–oxygen species modulate rate oscillations during dry reforming of methane

Check for updates

Luis Sandoval-Diaz [1] ✉, Daniel Cruz [1], Maurits Vuijk [1], Gianmarco Ducci [1], Michael Hävecker [1,2], Wulyu Jiang[1], Milivoj Plodinec [1], Adnan Hammud [1], Danail Ivanov[1], Thomas Götsch[1], Karsten Reuter[1], Robert Schlögl[1,2], Christoph Scheurer[1], Axel Knop-Gericke[1,2] & Thomas Lunkenbein [1]✉

When a heterogeneous catalyst is active, it forms metastable structures that constantly transform into each other. These structures contribute differently to the catalytic function. Here we show the role of different metastable oxygen species on a Ni catalyst during dry reforming of methane by combining environmental scanning electron microscopy, near ambient pressure X-ray photoelectron spectroscopy, on-line product detection and computer vision. We highlight the critical role of dissociative CO_2 adsorption in regulating the oxygen content of the catalyst and in CH_4 activation. We also discover rate oscillations during dry reforming of methane resulting from the sequential transformation of metastable oxygen species that exhibit different catalytic properties: atomic surface oxygen, subsurface oxygen and bulk NiO_x. The imaging approach allowed the localization of fluctuating surface regions that correlated directly with catalytic activity. The study highlights the importance of metastability and operando analytics in catalysis science and provides impetus towards the design of catalytic systems.

It is well accepted in the field of catalysis that the interaction of reactant molecules with the surface of a solid catalyst changes the structure of the active sites[1]. The catalytic cycle is closed when the products are desorbed and the sites are regenerated to the initial state. In this way, the active sites respond dynamically to the chemical stimulus. Observing this process with sufficient spatial (subnanometre) and temporal (subnanosecond) resolutions will yield valuable insights about the fundamental functioning of active catalysts. However, the spatial and temporal resolutions of most state-of-the-art techniques are still insufficient. Instead, we observe a superposition of spatial and temporal averages of the catalytic cycle[1]. In this sense, the active sites behave as metastable structures that continuously transform rather than adopting a single preferred state[2].

In catalytic reactors, combinations of kinetic and thermodynamic processes can produce metastable structures on large scales (microns, hours)[3,4]. Some examples are the coexistence of phases at a transition point[5], surface patterns[6–8], propagating chemical waves[9], spirals[10] and rate oscillations[11–14]. In this context, rate oscillations can be highly informative about the role of metastable structures in catalyst function[1,8]. Previous studies have aimed to understand the nature of oscillations in several reactions, including the oxidation of CO (refs. 6,12,15,16), H_2 (refs. 9,17), C_1–C_4 alkanes[14,18–23] and NH_3 (ref. 24), and the hydrogenation of CO (refs. 25,26), NO (ref. 27), NO_2 (ref. 10), acetylene[28] and nitrobenzene[4,29]. The occurrence of oscillatory behaviour has been reported on several metal catalysts, including Pt, Pd, Rh, Ir, Co and Ni over a broad range of operating conditions spanning from 1^{-10} to

[1]Fritz-Haber-Institut der Max-Planck-Gesellschaft, Berlin, Germany. [2]MPI for Chemical Energy Conversion, Mülheim a.d. Ruhr, Germany. ✉e-mail: lesandovaldi@fhi-berlin.mpg.de; lunkenbein@fhi-berlin.mpg.de

10^{-10} bar, and on various catalyst forms, including single crystals, foils, tapes, wires, foams and supported nanoparticles[4]. It was found that a sufficiently large number of active sites must fluctuate synchronously to produce detectable oscillations. This behaviour opens the way to exploring catalyst function correlations at current experimental resolutions, for example, with modern electron microscopes[30].

In this Article, we report an oscillating mode of dry reforming of methane (DRM; Supplementary Table 1 and Supplementary Equation 1) on Ni catalysts. Our goal is to understand how the processes occurring at the catalyst surface modulate DRM performance. In DRM, carbon dioxide (CO_2) and methane (CH_4) are converted to valuable syngas ($H_2 + CO$) of a H_2/CO ratio of 1 (refs. [31–33]). This product is suitable for the hydroformylation of olefins, the direct synthesis of acetic acid and dimethylether, or Fischer–Tropsch to olefins[32]. DRM requires a metallic catalyst such as Ni or Co and operating temperatures typically above 750 °C due to its high endothermicity (Supplementary Equation 1). In addition, the reaction is prone to deactivation due to coking, particularly at pressures above atmospheric. These limitations have prevented DRM from reaching industrial levels. We found that several forms of oxygen coexisted at the catalyst during the reaction, including adsorbed surface oxygen, subsurface oxygen and bulk oxide phases. Our results show that these forms of oxygen were metastable and exhibited distinct degrees of catalytic activity. Their sequential interconversion gave rise to the oscillations. Overall, our investigation unravels the role of metastable structures in catalytic activity.

Results

Individual effects of gaseous reactants

We studied the reaction by environmental scanning electron microscopy (ESEM) imaging coupled with on-line product detection[17,34,35]. In ESEM, image intensity and contrast depend mainly on surface morphologies, crystallographic orientations, compositions and adsorbates, that is, the surface chemistry, and also on external conditions such as temperature and gas environment[35]. We also used near ambient pressure X-ray photoelectron spectroscopy (NAP-XPS), post-catalytic structural evaluation and computer vision[36] of the ESEM images to supplement the research. With this approach, we directly imaged the working catalyst and identified surface regions of distinct catalytic performance.

First, we investigated the effect of H_2, CO_2 or CH_4 exposure on the catalyst surface at relevant DRM temperatures (Fig. 1 and Supplementary Table 2). We reduced a Ni foil in the ESEM reactor in a H_2:Ar mixture at 810 °C for 1,200 min. Figure 1a shows that the reduced catalyst surface was flat and polycrystalline, with micrometre-sized domains seemingly without any preferential orientation[17,35].

The H_2 flow was then replaced by CO_2 under isothermal conditions. This gas exchange is indicated by an arrow in Fig. 1a. The exchange resulted in the formation of bright features on the Ni surface. In an additional experiment, the H_2 flow was replaced by CH_4 after the catalyst had been reduced. No changes were observed on the surface after this exchange, as shown in Fig. 1b.

Complementary NAP-XPS analyses indicate the reduced state of the catalyst during the H_2 treatment (Supplementary Fig. 1a). The exchange of H_2 with CO_2 (Supplementary Fig. 1b) resulted in increasing O 1s signals and the transition from Ni^0 (Ni 2p binding energy, BE 852.4 eV) to Ni^{2+} (BE 856.2 eV). Closer examination of the O 1s spectra recorded in the CO_2:Ar atmosphere (Supplementary Fig. 2a and Supplementary Table 3) reveals at least two contributions centred at BE of 529.9 eV and BE of 531.3 eV, respectively. The peak at 529.9 eV can be attributed to oxygen in bulk NiO or to atomic oxygen adsorbed on the metallic surface[11,37]. The signal at 531.3 eV has been attributed to $Ni(OH)_2$, $Ni_{2-x}O_{3-y}$, NiOOH (refs. [37–39]) or to oxygen species adsorbed on structural defects[39]. This contribution has also been attributed to subsurface oxygen species[38,40]. Throughout the manuscript, we refer to NiO_x phases as oxides to distinguish them from the other O/Ni
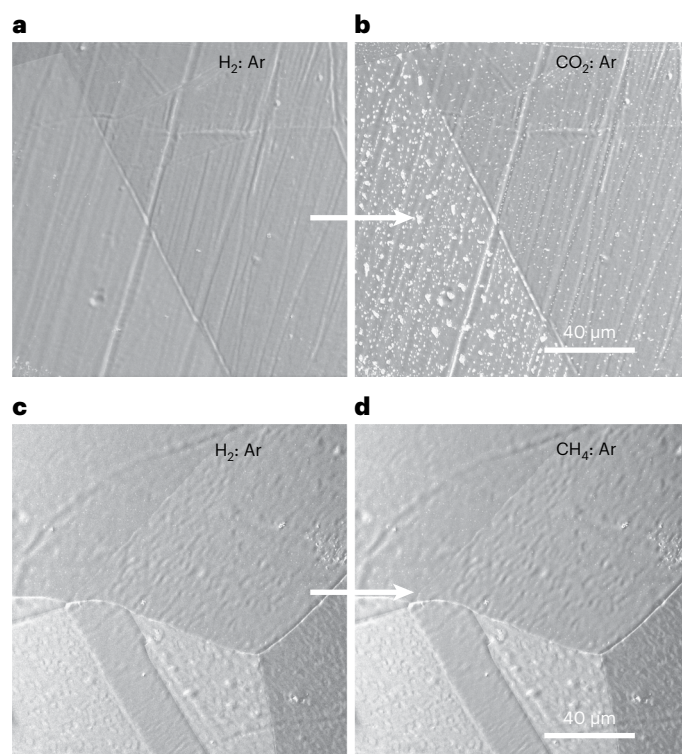
Fig. 1 | Gas composition influenced the surface morphology of Ni catalysts. **a**, ESEM image of a reduced Ni foil in H_2. Conditions of acquisition: gas mixture composed of 0.3 ml_N min^{-1} Ar, 0.6 ml_N min^{-1} H_2, 1,200 min of treatment. **b**, ESEM image of a reduced Ni foil exposed to CO_2 feed. Bright features occur at the catalyst. Conditions of acquisition: gas mixture composed of 0.3 ml_N min^{-1} Ar, 0.6 ml_N min^{-1} CO_2, 30 min of exposure to the feed. **c**, ESEM image of a reduced Ni foil catalyst in H_2. Conditions of acquisition: gas mixture composed of 0.3 ml_N min^{-1} Ar, 0.6 ml_N min^{-1} H_2, 1,200 min of treatment. **d**, ESEM image of a reduced Ni foil exposed to CH_4 feed. No changes are evident at the catalyst. Conditions of acquisition: gas mixture composed of 0.3 ml_N min^{-1} Ar, 0.6 ml_N min^{-1} CH_4, 30 min of treatment. Reaction temperature: 810 °C. Reaction pressure: 16 Pa. Imaging voltage: 10 kV. Arrows indicate the gas exchange. Supplementary Table 2 lists the conditions of acquisition used for generating this figure.

species. An additional spectral contribution centred at 532.7 eV can be attributed to SiO_x impurities. In short, the Ni catalyst under CO_2:Ar feed exhibited oxygen species that could be classified as bulk NiO_x, surface oxygen (O_s–Ni), subsurface oxygen (O_{subs}–Ni) and inert SiO_x (Supplementary Table 3).

Based on this interpretation, we attribute the growing bright features in Fig. 1a to NiO_x phases that formed by the oxidation of the catalyst with CO_2. The presence of these oxides can be detected from the ESEM average image intensities over the field of view. Increasing average image intensities indicate the accumulation of oxides on the surface of the catalyst.

No changes in the spectra were detected when the H_2 flow was exchanged with methane (Supplementary Fig. 1c). Indeed, the NAP-XPS measurements did not detect any carbon species at the surface in either CO_2 or CH_4 atmospheres. This observation excludes the presence of carbonates, carbonyl or carbide phases, and adsorbed species such as CO_2, CO or CH_x fragments.

Catalytic activation in DRM feed

Next, we investigated the catalyst behaviour under DRM feed (CO_2:CH_4:Ar) in a temperature regime between 700 °C and 900 °C. For clarity, we assign a time on stream (TOS) of 0 min to the instant when the catalyst temperature in the ESEM reactor was stabilized at 700 °C. The results are summarized in Fig. 2 and Supplementary Fig. 3.
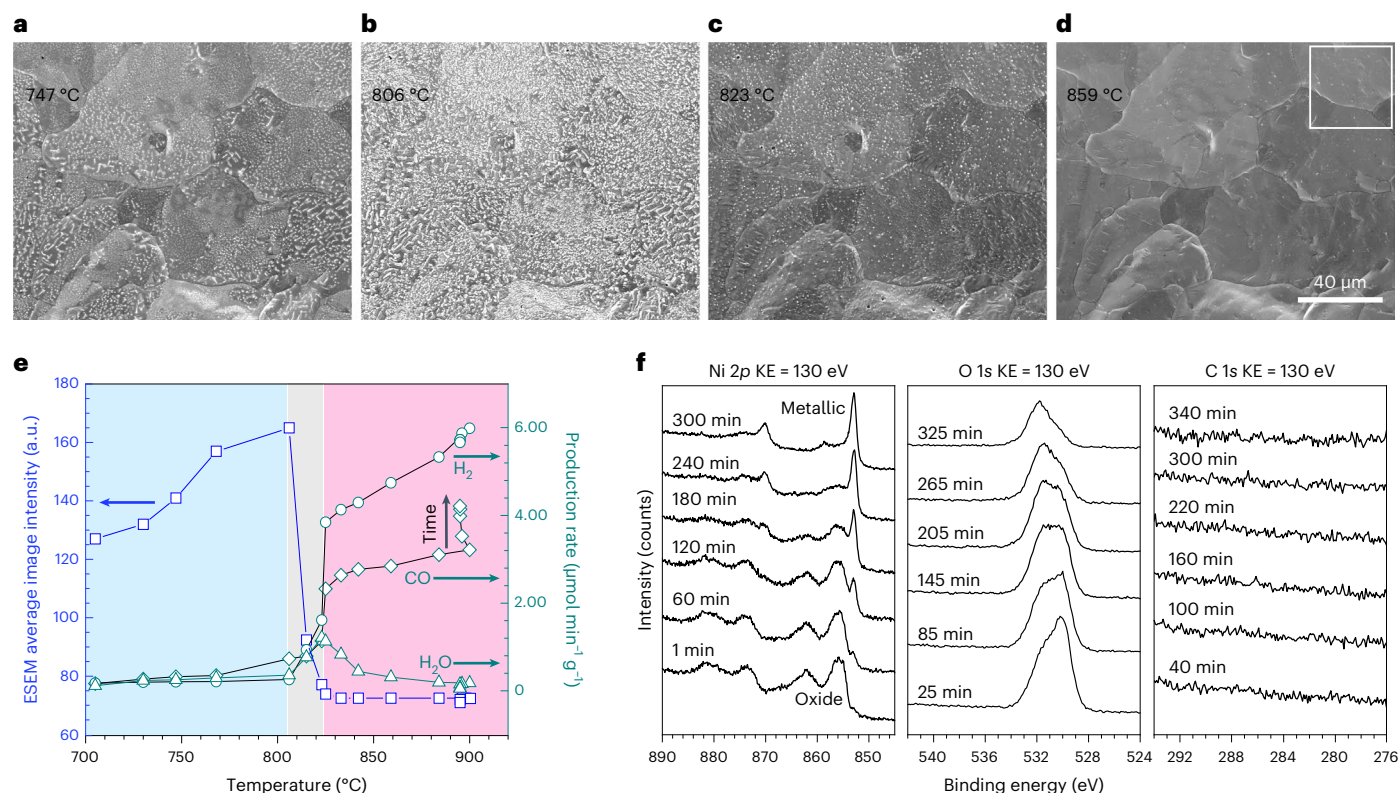
Fig. 2 | A redox transition at the Ni catalyst was characteristic during DRM activation. a–d, Consecutive ESEM images of the surface of a Ni foam taken at increasing reaction temperatures. The reaction temperature was 747 °C in **a**, 806 °C in **b**, 823 °C in **c**, and 859 °C in **d**. The square in **d** represents a selected ROI (Fig. 3). Conditions of acquisition of **a–d**: gas mixture composed of 0.3 ml$_N$ min^{-1} Ar, 0.3 ml$_N$ min^{-1} CO_2, 0.4 ml$_N$ min^{-1} CH_4. Imaging voltage: 10 kV. **e**, Correlation between the average image intensity and product formation rates as a function of temperature. The blue area marks the low-temperature regime. The grey area marks the redox transition regime at the catalyst and the catalytic activation. The pink area marks the high-temperature regime. Re-evaluated from ref. 34. **f**, NAP-XP spectra of Ni 2p, O 1s and C 1s core levels at kinetic energies (KE) of 130 eV in DRM feed at 810 °C. Conditions of acquisition: gas mixture composed of 0.3 ml$_N$ min^{-1} Ar, 0.3 ml$_N$ min^{-1} CO_2, 0.4 ml$_N$ min^{-1} CH_4. Reaction pressure: 16 Pa.

Figure 2a,b shows that the catalyst surface developed bright features, that is, NiO_x phases, in the temperature range of 700–808 °C. At higher temperatures, these oxides were consumed (compare Fig. 2b,c and Supplementary Fig. 3). The transition to a metallic catalyst surface was apparently completed at 825 °C. The catalyst remained in this state (Fig. 2d) during the subsequent heating to 900 °C.

We investigated the correlation between catalyst state and DRM performance at different temperatures. Below 808 °C (Fig. 2e, blue area), increasing ESEM image intensities were detected, indicating a gradual accumulation of oxides at the surface. In this regime, the formation of H_2, CO and H_2O was low and the H_2/CO ratio was below 1. Between 808 °C and 825 °C, the ESEM image intensities decreased abruptly (grey area of Fig. 2e and Supplementary Fig. 3), indicating the consumption of oxides. Simultaneously, the production of water and syngas was initiated with relative magnitudes following the order H_2 > CO > H_2O. With increasing temperature (red area of Fig. 2e), H_2O formation ceased and the H_2/CO ratio approached 1 after treating the catalyst for 1,000 min at 900 °C (Supplementary Fig. 3). Further details can be found in ref. 34.

We investigated the surface chemistry during DRM by NAP-XPS measurements (Fig. 2f and Supplementary Fig. 2b). Analysis of the O 1s spectra shows similar oxygen species at the catalyst in either CO_2:Ar or DRM feeds (Supplementary Fig. 2 and Supplementary Table 3). During catalytic ignition, the overall intensity of the O 1s signals decreased with the reduction of nickel. These spectra show that the oxygen species at BE of 529.9 eV (NiO_x, O–Ni$_{(s)}$) was being consumed faster than the species at BE of 531.3 eV (O–Ni$_{(subs)}$). Both forms of oxygen were still present at the catalyst after 325 min of syngas production. Notably, the reduction of Ni appeared to be complete after this prolonged treatment

(Fig. 2f). In addition, no carbon species were detected on the surface during syngas production (Fig. 2f).

The gas signals in the NAP-XPS experiment followed the same trends as measured in the ESEM reactor (Supplementary Fig. 4). In summary, both experiments indicate the same behaviour. Oxidation of the catalyst and low activity dominated below 808 °C. The catalytic activation occurred at temperatures slightly above 808 °C. This activation was accompanied by catalyst reduction. A metallic catalyst surface dominated during the high-activity regime at much higher temperatures. The spectra show that oxygen species remained at the active metallic catalyst after several hours of syngas production.

Rate oscillations

After 1,000 min at 900 °C under DRM conditions in the ESEM reactor, the catalyst temperature was reduced to 808 °C (Supplementary Fig. 3). Surface oxides reappeared when the temperature dropped below 825 °C. In addition, the system started to oscillate at time on stream (TOS) 1,879 min, with a period of ~93 min, although the pressure, heating power and gas feeds were kept constant.

Supplementary Video 1 illustrates the catalyst dynamics during the oscillations. The video shows that oxide islands grew at discrete locations of the surface, which shrank and then grew again. This redox cycle is the most obvious behaviour of the catalyst surface during the oscillations. Furthermore, the cycling of the oxides occurred over all the micrometre-sized domains of the metallic catalyst with no apparent preference.

The selected region of interest (ROI) of Supplementary Video 2 shows that the catalyst surface that remained uncovered by oxides
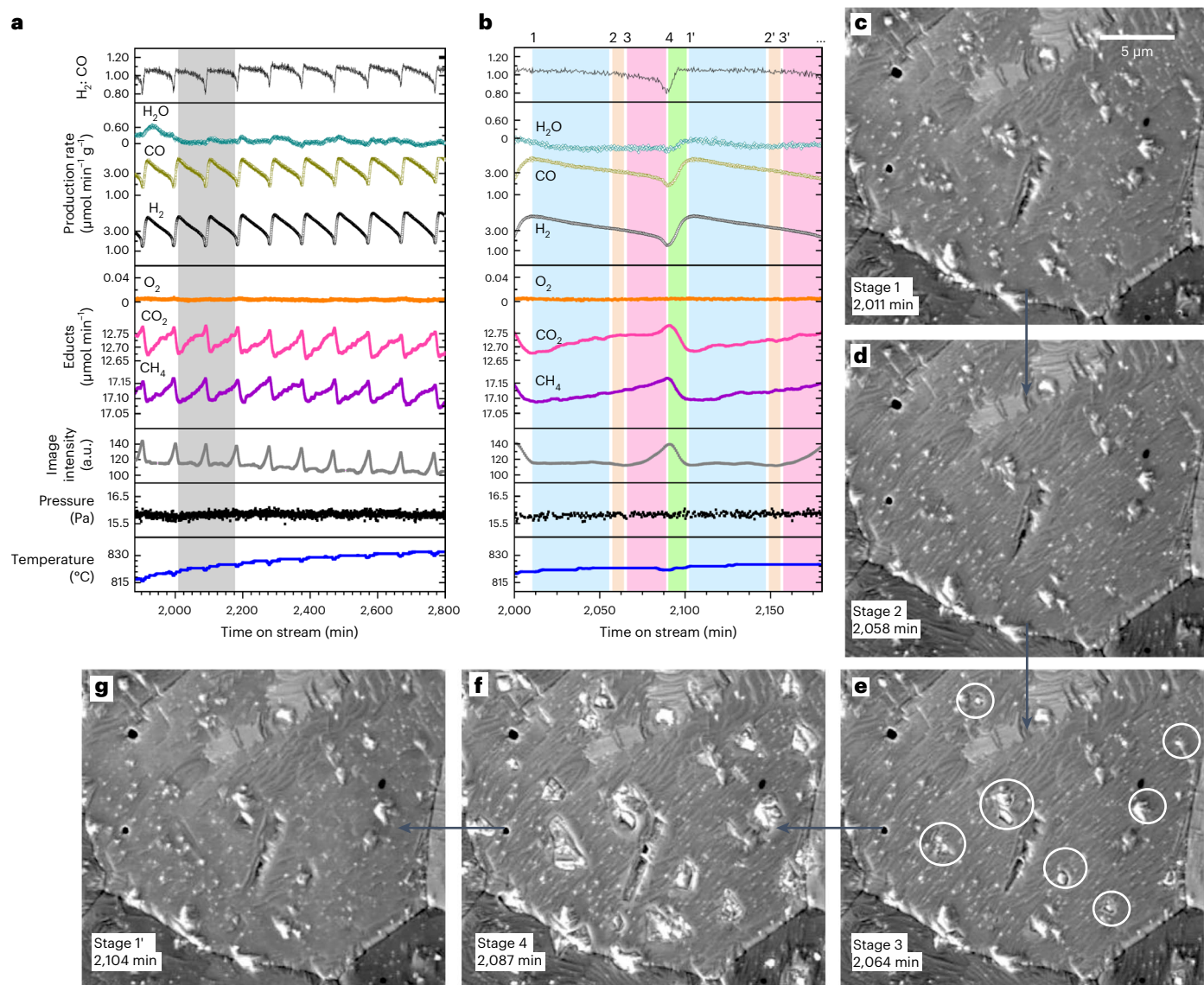
Fig. 3 | Self-sustained oscillations of DRM occurred on a Ni catalyst. a, Time series of the temperature, reactor pressure, average image intensities and mass spectrometry signals of reactants and products during the oscillations, which occur over a Ni catalyst foam. **b**, Magnified region taken from the grey-highlighted dataset in **a**. The stages of the oscillation cycle are marked in the horizontal axis. **c–g**, Catalyst surface evolution during the oscillation cycle as shown in **b**. **c**, ESEM image of the catalyst surface at Stage 1 and TOS 2,011 min.

d, ESEM image of the catalyst surface at Stage 2 and TOS 2,058 min. **e**, ESEM image of the catalyst surface at Stage 3 and TOS 2,064 min. **f**, ESEM image of the catalyst surface at Stage 4 and TOS 2,087 min. **g**, ESEM image of the catalyst surface at Stage 1' and TOS 2,104 min. The images were extracted from the ROI highlighted in Fig. 2d. Arrows denote increasing TOS. Circles in **e** denote areas of oxide growth. Conditions of acquisition: gas mixture composed of 0.3 ml_N min^{-1} Ar, 0.3 ml_N min^{-1} CO_2, 0.4 ml_N min^{-1} CH_4. Imaging voltage: 10 kV.

went through cycles of roughening and smoothening. Starting from a smooth surface, the catalyst became rough. Subsequently, the oxides began to grow. The oxides reached their maximum size on the roughened surface, and then they rapidly shrank. The metallic surface smoothened again as the oxides shrank.

The DRM activity also oscillated with the redox cycles of the catalyst. The time series of reactants, products, H_2/CO ratios and ESEM average image intensities representing oxide contents are shown in Fig. 3a. Minima in the production rates coincided with maxima in the ESEM average image intensities. Similarly, maxima in the production rates coincided with minima in the ESEM average image intensities.

Phenomenologically, we describe the oscillations in terms of four stages that can be traced between the successive cycles. These stages are highlighted in Fig. 3b and in the ESEM images of Fig. 3c–h.

At stage 1, the H_2/CO ratio was 1, the ESEM image intensity (oxide content) was at a minimum and the catalytic conversion was at its maximum. Some parts of the metallic surface that remained uncovered by oxides were smooth (Fig. 3c), but small oxide nuclei were already present. The syngas production started to deactivate slowly in the subsequent time (Fig. 3b, blue area).

At stage 2, the metallic surface was roughened (Fig. 3d) and the H_2/CO ratio decreased slightly. Although slight deactivation still dominated at this stage, the activity changes were not abrupt (Fig. 3b, orange area).

Stage 3 was characterized by oxide growth (Fig. 3e, circles), rapid catalytic deactivation and a further decrease in the H_2/CO ratio (Fig. 3b, pink area).

At stage 4, the oxide islands reached their maximum sizes (Fig. 3b,f). The catalytic conversion was at a minimum and the H_2/CO ratio reached its lowest values (~0.80).

Subsequently, the syngas production was rapidly reactivated. This process was accompanied by a rapid shrinkage of the oxides and smoothening of the surface (Fig. 3g, green area of Fig. 3b). The product
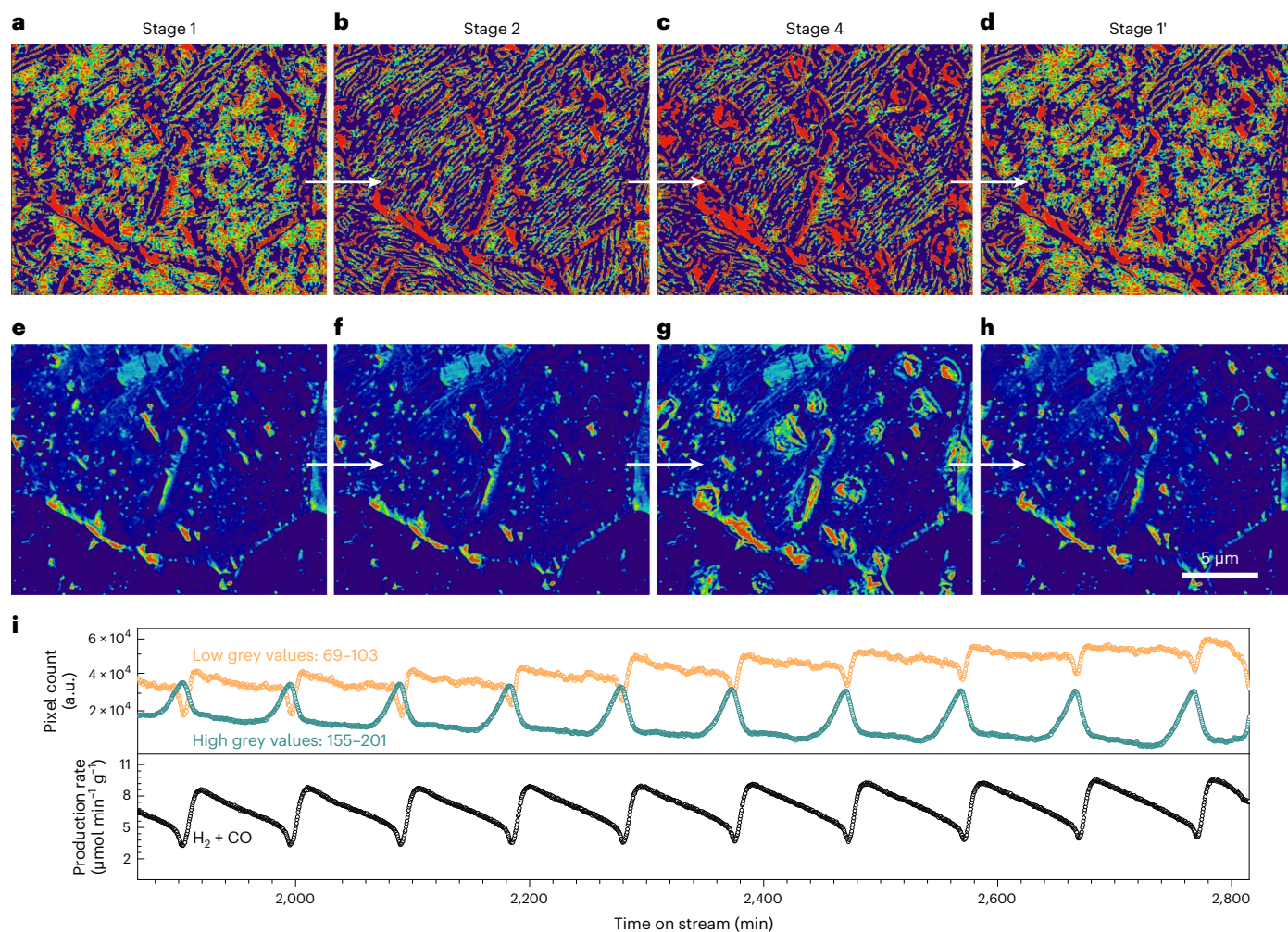
Fig. 4 | Grey value segmentation of ESEM images correlated to activity.
a–d, Artificially coloured ESEM images representative of low grey values (69–103) over an oscillation cycle: segmented image representative of stage 1, where yellow/light-green regions correspond to surface portions contributing to the histogram in this grey values range (69–103) (**a**); segmented image representative of stage 2 displays the vanishing of the yellow/light-green regions at the metallic surface during surface roughening (**b**); segmented image representative of stage 4 at the highest oxide coverages displays minimum contents of yellow/light-green regions at the metallic surface (**c**); segmented image representative of stage 1′ displays the reappearance of the yellow/light-green regions at the metallic surface after reactivation (**d**). **e–h**, Artificially coloured in situ ESEM images representative of high grey values (155–201) over an oscillation cycle: an image representative of stage 1, where light regions correspond to the surface portions contributing to the histogram in this range (155–201), that is, oxides (**e**); segmented image representative of stage 2 during surface roughening (**f**); segmented image representative of stage 4 at maximum oxide coverages displays growth of oxide islands (**g**); segmented image representative of stage 1′ displays shrinking of oxide islands and closure of the oscillation cycle (**h**). **i**, Time series of the number of pixels contributing to low and high grey values during the oscillations and its correlation to syngas production rate. The low grey values (69–103) representative of metallic regions correlate to the reaction performance, while the high grey values (155–201) representative of oxides exhibit an opposite behaviour.

ratio regained a value of 1. These processes brought the system back into a state (stage 1′) similar to stage 1. These events mark an oscillation cycle.

The catalyst temperature increased on average by ~15 °C during the 16.7 h of observation of the oscillations. In addition, each oscillation cycle was accompanied by a negative temperature peak of ~1 K that coincided with the maximum of the oxide coverage. Compared with the other gas products, the periodicity and productivity of water were not pronounced. We detected only a slight increase in its signal during the rapid reactivation step of oxide reduction.

Additional phenomena not considered in the previous analysis may still be hidden in the images of the oscillating catalyst surface. To investigate this aspect, we calculated the histograms of the individual frames of Supplementary Videos 1 and 2. As the surface features have distinct grey values, we can classify the features according to their position on the grey scale. For example, the oxide islands occur closer

to the bright end of the scale compared to the metallic substrate. As shown in Supplementary Fig. 5 and in Supplementary Video 3, we have fitted the histograms of the ESEM frames by Gaussian functions centred on given grey values.

Supplementary Video 3 shows the behaviour of the fitting functions during the oscillations. The function indicative for the low grey values (grey values: 69–103) was characterized by an oscillating intensity profile. The function describing the high grey values (grey values: 155–201) showed first an increase in intensity while the profile moved towards higher grey values. This is followed by a decrease in intensities and a shift of the distribution towards low grey values.

We separated the low grey contribution (grey values: 69–103) from the high grey contribution (grey values: 155–201) by pixel filtering. Chemically, the low grey contribution represents the parts of the catalyst not covered by oxides. Supplementary Video 4 shows the result when only the low grey pixels from the data of Supplementary Video 2

are displayed. We have added artificial colouring to highlight the surface changes. The video shows that some regions of the surface (yellow/light green) fluctuated rapidly, forming layer-like surface regions. The video also highlights that the coverage of these layer-like regions changed during the oscillations. Selected frames are depicted in Fig. 4a–d to better understand how these regions correlate to the different stages of the oscillation cycle discussed in Fig. 3. At stage 1 (Fig. 4a) a high coverage of this surface layer was observed, which remained until stage 2, when surface roughening led to a rapid depletion of this layer (Fig. 4b). At stage 4 (Fig. 4c, highest oxide content), this layer was only minimally present and rapidly increased again during the subsequent reactivation. The layer was fully restored at stage 1′ (Fig. 4d).

In addition, Supplementary Video 5 highlights the behaviour of the high grey pixels corresponding to the oxide phases (light-green regions) over the substrate (dark-blue background). Selected frames are reproduced in Fig. 4e–h. A series of video images following this process in a magnified ROI (Supplementary Video 6 and Supplementary Fig. 6) suggests that the oxide growth began around small oxide nuclei that were already present at the surface. Subsequently, the contraction of the oxides initiated at the outer perimeter of the islands. During catalytic reactivation, the oxide island rapidly disintegrated into smaller particles and eventually the phase was consumed, leaving only small nuclei on the surface.

The intensities of these low and high grey values contributions during the oscillations are shown in Fig. 4i. These intensities are proportional to the number of pixels of the respective grey levels of the image. Although the contributions of low grey and high grey values oscillated in phase, their behaviour was opposite. The curve of the low grey values resembles the shape of the syngas productivity, which was added for comparison. In contrast, the high grey values (oxide islands) correlate negatively with syngas productivity. Based on this result, the low grey values could be interpreted as active surface areas important for syngas production.

Supplementary Video 7 shows the growing/shrinking oxide boundaries across the field of view of Supplementary Video 1. The metallic substrate was removed using a wavelet algorithm. We have also superimposed an arrow indicating the direction of the gas flow in our reactor. The propagation of oxide growth/shrinking across the surface coincides with the direction of the gas flow, suggesting that separate regions of the oscillating catalyst were synchronized by gas phase coupling[4]. Oxidation fronts propagated upstream, and reduction fronts propagated downstream.

Finally, we analysed a cross-section of the post-reaction catalyst prepared by focused ion beam milling combined with transmission electron microscopy (Supplementary Fig. 7 and Supplementary Note 1). The analysis reveals the penetration of oxygen several hundred of nanometres below the catalyst surface and a strained structure at the catalyst bulk.

Discussion

Our combined operando ESEM/NAP-XPS observation supports the activation of CO_2 over smooth metallic Ni surfaces (Fig. 1a and Supplementary Fig. 1b), while CH_4 was found to be unaffected by the reduced surface (Fig. 1b and Supplementary Fig. 1c). It is generally discussed in the literature that CH_4 activation occurs by scission of the $H_3C–H$ bond, followed by cascading into CH_x^* ($0 \leq x \leq 3$) fragments[41–44]. As CH_4 has the strongest C–H bond among hydrocarbons (439 kJ mol^{-1})[41–43], this activation path requires high-energy sites[45]. Nevertheless, we found no evidence of carbon species during the treatment with CH_4, at least within our experimental resolution. In fact, co-feeding of CO_2 was required for CH_4 conversion. These results suggest that CO_2 was assisting the activation of CH_4 in a different reaction path than methane cracking. This possibility is consistent with previous results suggesting that oxygenate species may be key to CH_4 activation[45–47]. The different

Table 1 | A compilation of the chemical reactions describing DRM activity on the nickel catalyst

Equation number	Chemical reaction	Description
1	$CO_2 + Ni_s \leftrightarrow O_s–Ni + CO$	Dissociative adsorption of CO_2
2	$O_s–Ni + Ni_s \leftrightarrow Ni_s + O_s–Ni$	O surface diffusion
3	$O_s–Ni + Ni_{subs} \leftrightarrow Ni_s + O_{subs}–Ni$	O diffusion into subsurface
4	$O–Ni_{subs} + Ni_{subs} \leftrightarrow Ni_{susb} + O_{subs}–Ni$	O subsurface diffusion
5	$O_s–Ni \leftrightarrow NiO_x$	NiO_x formation
6	$O_{subs}–Ni \leftrightarrow NiO_x$	NiO_x formation
7	$CH_4 + O_s–Ni \leftrightarrow Ni_s + CO + 2H_2$	Activation of CH_4
8	$CH_4 + NiO_x \leftrightarrow Ni + CO + 2H_2$	NiO_x reduction by CH_4
9	$H_2 + NiO_x \leftrightarrow Ni + H_2O$	NiO_x reduction by H_2

Subscript 's' denotes a surface site; subscript 'subs' denotes a subsurface site.

reactivities of these oxygenate species under reaction conditions (Table 1) can also explain the main results of the present study.

Initially, CO_2 dissociation leads to the formation of $O_s–Ni$ (equation (1)) and gaseous CO. Previous studies[48,49] have suggested that $O_s–Ni$ is mobile (equation (2)) and can dissolve into the metallic bulk at the high temperatures of DRM, leading to the formation of $O_{subs}–Ni$ (equation (3)). This is consistent with our post-catalytic analysis showing the presence of oxygen deep in the catalyst bulk (Supplementary Fig. 7) and with previous reports that found an oxygen-rich region extending several hundred nanometres into the bulk of the catalyst[11,38]. This form of oxygen is essentially inactive to DRM as it is not in contact with the gaseous reactants. It can therefore accumulate as an inactive buffer species. Eventually, $O_s–Ni$ and $O_{subs}–Ni$ transform into NiO_x phases (equations (5) and (6)). The activation of CH_4 was initiated by reactions with the oxygen species present at the surface of the catalyst (equations (7) and (8)).

Furthermore, the equations of Table 1 also provide a reasonable framework for understanding the temperature dependence of the catalytic reaction. For example, at temperatures below the redox transition, equation (1) could occur at faster rates than equations (7) and (8). As a result, the excess oxygen is not transferred to the gas product fast enough and accumulates in the catalyst, mainly as $O_{subs}–Ni$ and NiO_x (equations (3)–(6)). At temperatures well above the oxide-to-metal transition, equations (7) and (8) become fast enough to efficiently transfer the stored oxygen to gaseous products, favouring a metallic-like catalyst state.

At temperatures around the phase transition, the rates of equations (1)–(8) could kinetically trap the system in the oscillatory regime. We summarize this process schematically in Fig. 5, where we interpret the oscillations in terms of the relative rates of these reactions. At stage 1, equations (1) and (7) are almost balanced, leading to a syngas of ratio 1. Chemically, the $O_s–Ni$ formed by equation (1) is rapidly consumed by equation (7). The active surface at this stage can be viewed as a process with high turnover between equation (1) and equation (7). This behaviour is consistent with the surface regions highlighted in Supplementary Video 4 and in Fig. 4a–d.

However, some part of the surface oxygen leaks into the subsurface via equation (3). This circumstance implies that equations (3) and (7) are competitive reactions that modulate the availability of surface $O_s–Ni$. The reason for this behaviour is the intrinsically high reactivity of $O_s–Ni$, which cannot be stabilized at the surface and therefore evolves into the gas product via equation (7) or into unreactive $O_{subs}–Ni$ species. Hence, the leakage of $O_s–Ni$ into the subsurface reduces the rate of equation (7). We see this effect as a deactivation in the syngas productivity during
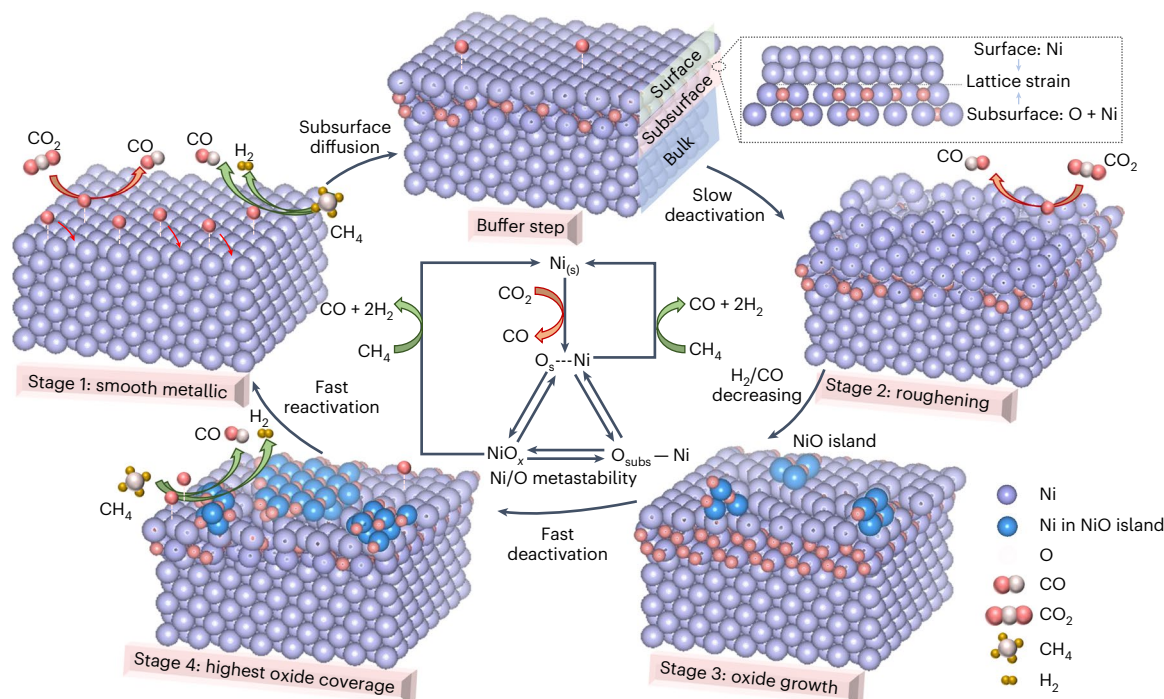
Fig. 5 | Metastability of oxygen species on a Ni catalyst induced oscillatory behaviour. Schematics summarizing the chemical equations presented in Table 1, featuring surface oxygen formation, subsurface diffusion, oxide formation and fast regeneration in the oscillatory cycle. The central part of the figure displays the reduced kinetic cycles of DRM and depends on the catalyst history.

the time after stage 1 (Fig. 5). Consequently, the coverage of the fluctuating layer shown in Fig. 4a–d and Supplementary Video 4 decreases during this deactivation, indicating a decrease in O_s–Ni.

The presence of oxygen several hundred nanometres below the surface (Supplementary Fig. 7 and Supplementary Note 1) gives an idea of the extent of this leakage. The structure in this bulk-like region was found to be highly distorted, indicating the accumulation of strain in the catalyst substrate. It has been suggested that an accumulation of distortions in the bulk could lead to large-scale effects such as reshapings/roughenings of the surface[9]. Thus, diffusion of oxygen into the subsurface can also explain the surface roughening characteristic of stage 2. Surface roughening can expose new metallic sites that favour equations (1) and (3) over equation (7), leading to an increased rate of oxygen uptake and a decrease of the H_2/CO product ratio (Fig. 5).

Eventually, the subsurface region becomes locally saturated with oxygen and oxide phases begin to crystallize at stage 3. At this point, the catalyst temperature drops by ~1 K, which may reflect a slightly endothermic crystallization of NiO_x. Our results in Supplementary Fig. 6 demonstrate that oxide formation follows a nucleation and growth mechanism similar to the crystallization of solids from oversaturated solutions[50], in this case from a solid O/Ni solution. As the oxide nuclei do not disappear completely during the oscillations, the oxides can grow at similar positions during the successive cycles.

When the oxide islands reach their maximum size at stage 4, they rapidly disintegrate into small pieces and syngas production is reactivated (Fig. 5). This reactivation is controlled by the reduction of NiO_x, apparently without further catalyst oxidation by equation (1). This process produces syngas with excess amounts of H_2, indicating the dominance of equation (8). As a result, the H_2/CO ratio increases. At this point, small amounts of water are formed (Figs. 3a,b), possibly as a result of methane over-oxidation by the oxide. This observation may also indicate that part of the syngas may have reacted downstream with the remaining oxide (equation (9)). This effect could stimulate further reduction and fast coupling of the oscillation along the reactor, and

could also be the reason for the slight temperature increase observed during reactivation of the catalyst (Fig. 3 and Supplementary Videos 1 and 7). A key observation during reactivation is the recovery of the fluctuating surface layer (Fig. 4 and Supplementary Video 4). We interpret this result as the regeneration of the active O_s–Ni phase. The result of this process brings the catalyst to a metallic-like state of high activity, similar to stage 1.

The structural details of the reactivation process that returns the system to the most active stage may require further operando investigation. A previous study of NiO_x reduction by methane[51] has found surface morphologies similar to our spent catalyst (Supplementary Fig. 8 and Supplementary Note 2). The authors argued that the reduction of NiO_x could produce metallic nuclei or even atomic Ni species at the oxide/substrate interface. These sites could be very active for methane activation. We also found that the metallic substrate was severely roughened when oxide islands started to grow. This deformed substrate could be a poor template for excessive oxide accumulation, as previously suggested[52]. At some point, the mismatching lattices can lead to active local defects and structural instabilities in the oxide phase. In brief, NiO_x phases become unstable under the reaction conditions due to lattice mismatch, local saturation and the creation of reactive sites. Consequently, this phase spontaneously reverts to O_s–Ni, which closes the oscillation.

Our observations lead to the interpretation that the different forms of O/Ni species are intrinsically metastable under DRM conditions. We propose that such metastability is the cause of the oscillations that gives rise to a chain of events that kinetically acts upon itself (Fig. 5, centre). The different forms of O/Ni have distinct levels of activity and transform into each other through the influence of equations (1)–(8). Thus, the system remains sequentially in chemical states of different performances rather than in a preferred steady state regime. In this sense, the behaviour of the catalyst during the oscillations can be seen as a continuous frustrated phase transition that cannot be completed in any direction[1,2].

We contrast our study with reports of methane oxidation with O_2 over various transition metals. In these studies, the reaction was

reactivated by the reduction of oxides[53–56]. In addition, a study of oscillations during propane oxidation over Ni catalysts suggested the involvement of oxygen dissolution into the Ni substrate as a key ingredient of the oscillatory cycle[11]. This solid solution of oxygen in nickel has been proposed as a buffer step that delays the transition between low-activity oxides and high-activity metallic states. Our results confirm these observations.

We note that the oscillations of these studies exhibited large temperature fluctuations that could thermokinetically synchronize the surface states, in contrast to the temperature fluctuations of ~1 K detected here. We speculate that these small temperature fluctuations imply that the chemical potentials of the metastable O/Ni phases were almost identical during the oscillations. This hypothesis requires further validation. We hope that these results will stimulate future scientific enquiries into the likelihood of oscillatory dynamics in real isothermal reactors that can clarify the importance of thermokinetic coupling for synchronization and the influence of metastable states on general catalytic behaviour.

In conclusion, our study revealed an oscillatory behaviour of DRM over Ni catalysts. Three interconverting oxygen forms were identified in the metastable ensemble, which was found to be the most relevant element of the oscillations. The dissociative activation of CO_2 sourced these different forms of oxygen, which were distinctly reactive towards methane.

A fluctuating layer on the metallic Ni surface was identified as the state representative of high DRM activity. This layer was detected using a computer vision approach based on image segmentation. This layer is proposed to be a collection of active sites with high turnover frequencies, in which O_s–Ni is the dominant state. Diffusion of oxygen from this layer into the subsurface led to deactivation and the subsequent growth of oxides. The cycle was closed by spontaneous recovery of the active layer by decomposition of the oxide phase in the chemical environment. The system was effectively synchronized by gas phase coupling, highlighting the importance of reactor design for subsequent studies of non-linear dynamics in catalysis.

The metastability of the O/Ni system provides insight into future design concepts where the goal is to stabilize the active state with minimal energetic compromise. For DRM, this could be achieved by co-feeding more potent oxidants such H_2O or N_2O (ref. 57) or by a bimetallic architecture[58] aimed at locally concentrating the amount of active O_s–Ni. Another option would be to eliminate the possibility of O_s–Ni leakage into the bulk, for example, through nanoparticles or thin film technologies.

Overall, the study highlights operando investigations to extend our knowledge of heterogeneous catalysis for prospective design concepts based on mechanistic understanding. We also highlight that the oscillatory regime was limited within a certain range of experimental parameters, for example, the temperature. For a deeper understanding of the asymptotic behaviour of the reactions, a dedicated study should be carried out and is left for future work. This approach may include further tailored experiments, density functional theory calculations of the reaction paths proposed in Fig. 5 and numerical solutions of the kinetic model to address the bifurcation behaviour.

Methods

Operando ESEM set-up
A sample of the metallic Ni catalyst was positioned inside a customized flow reactor compatible with ESEM imaging. A gas mixture at 16 Pa was fed into the reactor, and the catalyst was heated by an infrared laser. ESEM images were typically acquired at 7.5–10 kV under different gas compositions and catalyst temperatures.

Our set-up features a quartz tube reactor inside the chamber of a commercially available environmental SEM (ESEM, FEI 200 Quanta FEG) lined to a quadrupole mass spectrometer (QMS, 200 Prisma Pfeiffer)[34]. Changes at the catalyst and in gas phase compositions

are determined simultaneously, enabling the direct investigation of the influence of catalytic dynamics on performance. Our operando ESEM resembles a flow reactor that reproduces the flow pattern of laboratory- and industrial-scale systems, maximizes contact points between gas and solid phases, enables calibrations of gas compositions, and prevents contaminations stemming from the ESEM chamber environment. Temperature and gas phase compositions were controlled during surface imaging. We used a metallic Ni catalyst (foil or foam, 99.5% purity, Goodfellow) onto which a K-type thermocouple was spot-welded. Pure gases (Westfalen 5.0) were dosed into the quartz tube reactor by individual mass-flow controllers (Bronckhorst).

Images of the catalyst surface were acquired every 17.5 s with the large field detector of the ESEM at acceleration voltages of 7.5–10 kV and a chamber pressure of 16 Pa and a pixel depth of 8 bits (0–255 units on a grey values scale). In operando mode, catalytic rates of conversion and product selectivities were measured simultaneously to surface imaging[34].

Reference tests
Samples of the Ni catalyst (metallic foam, 35 mg) were treated for 1,200 min at 810 °C in an atmosphere composed of 0.6 ml$_N$ min^{-1} H_2 and 0.3 ml$_N$ min^{-1} Ar (where subscript 'N' indicates gas volumes at normal conditions). The chamber pressure was 16 Pa. Afterwards, the atmosphere composition was switched to either 0.6 ml$_N$ min^{-1} CO_2 and 0.3 ml$_N$ min^{-1} Ar, or 0.6 ml$_N$ min^{-1} CH_4 and 0.3 ml$_N$ min^{-1} Ar. ESEM video frames were collected during these treatments every 17.5 s.

Operando ESEM DRM tests
For this part, a metallic foam was used to maximize the surface area and reach detectable levels of catalytic conversion. After pre-treating the Ni catalyst foam for 1,200 min at 810 °C in an atmosphere composed of 0.6 ml$_N$ min^{-1} H_2 and 0.3 ml$_N$ min^{-1} Ar, the H_2 flow was switched off and the reactor was cooled down to room temperature. Flows of 0.4 ml$_N$ min^{-1} CH_4 and 0.3 ml$_N$ min^{-1} CO_2 were introduced in the reactor until the gas phase compositions in the QMS signals had stabilized. The catalyst was heated to 700 °C within 10 s, and after 10 min of stabilization, ESEM imaging was initiated (TOS 0 min). Due to imaging artefacts, the reaction temperature must be increased step by step in the ESEM reactor for a continual acquisition. We increased the temperature in this manner (6–17 °C per step) from 700 °C to 900 °C. After 1,000 min of dwelling at 900 °C, the reaction temperature was decreased to 818 °C. Oscillations initiated spontaneously (TOS 1,880 min). ESEM video frames were continually collected until the end of the experiment (TOS 2,821 min).

During oscillations, the signal of O_2 was found to be steady and close to zero, indicating its exclusion from the dynamics. O_2 often contaminates the microscope chamber due to external leaks. Consequently, obscuring dynamics initiated by oxygen-induced hydrocarbon oxidation can cause oscillating dynamics and disrupt the chemical network (Supplementary Table 1)[11].

Image treatment and video production
Collected ESEM video frames were treated with Fiji[59]. The stack of video frames was aligned with translation registration. Afterwards, average image intensities calculated by summing all of the pixel intensities and then dividing by the number of pixels in the field of view were plotted as a time series. Videos and a selected ROI cropped and digitally scaled from the video frames were produced with the same software (Supplementary Videos 1 and 2).

Image histograms were calculated from the video frames and fitted by Gaussian functions with a recurring algorithm implemented in Python. The fitting functions and original histograms were combined in a video file (Supplementary Video 3). Afterwards, the maximum and minimum ranges of grey values were adjusted from the original

video frames to segment the images according to low (69–103) and high (155–201) grey values contributions. A schematic representation of this procedure is shown in Supplementary Fig. 5. Finally, the resulting images were combined in separate videos and applied an RGB look-up table (Supplementary Videos 4 and 5). Digitally cropped areas from Supplementary Video 5 were used to produce Supplementary Video 6.

To isolate oscillating features from the image sequence, we employed an image filtering algorithm based on the fully separable discrete wavelet transform. This was implemented using Python and the PyWavelets package[60]. We treated the image sequence as 3D data with dimensions (x, y, t) and performed a 3D fully separable discrete wavelet transform using a Daubechies 2 'db2' wavelet. For each resulting channel, we calculated the overall energy of the channel as the absolute mean over its values. We used the geometric mean of the channel energies as a threshold value and excluded channels with energy values above the threshold from the reconstruction. This approach effectively isolates the lower-energy temporal components containing oscillating features from the static background. The filtered frames were combined in Supplementary Video 7.

Operando NAP-XPS

NAP-XPS measurements were performed at the UE56/2-PGM1 (Elliptical Undulator) beamline of the synchrotron radiation facility of BESSY II of Helmholtz-Zentrum Berlin, Germany. The details of the beamline layout and performance can be found elsewhere[61]. The home-built near-ambient pressure electron spectrometer is described in detail in the literature[62,63].

The nickel foam sample and a K-type thermocouple were fixed into a sapphire sample holder. The sample was mounted inside the XPS/XANES reaction cell, near to the aperture of the first differential pumping stage. The exit slit of the beamline was 180 um and a pass energy of 10 eV and 0.1 eV step were used during spectra acquisition with an experimental resolution of about 0.55 eV.

The heating treatment was carried out with a near-infrared laser (808 nm, maximum 60 W) shining at the rear of the mounting plate. Gas compositions during the measurements were monitored by a QMS (200 Prisma Pfeiffer).

The catalyst was pre-treated by annealing in 0.16 mbar (16 Pa) of H_2:Ar mixture at 810 °C using a heating rate of 5 °C min^{-1} to achieve the reduced state. The partial pressure of the gas feeds was controlled by mass-flow controllers (Bronkhorst) and set to the values of the operando ESEM experiments.

XP spectra of core level regions were recorded with kinetic energies of emitted photoelectrons at 130 eV and 300 eV for Ni $2p$ and 130 eV, 300 eV and 600 eV for O $1s$, C $1s$ and Si $2p$.

Afterwards, spectra were acquired on the pre-reduced sample at the same pressure and temperature with gas feeds of CO_2:Ar, CH_4:Ar and CO_2:CH_4:Ar. Each set of spectra was recorded with 60 min of separation between the first acquisitions to evaluate the changes over time.

XP spectra were analysed with CasaXPS. The binding energies were calibrated to the Fermi edge of an Au reference sample. The O $1s$ spectra were deconvoluted with combined Gaussian and Lorentzian functions after a Shirley + linear background subtraction.

Note that besides employing two independent operando characterization techniques (NAP-XPS and ESEM) that reveal the same chemistry, operando experiments are advantageous over in situ experiments as they help precluding imaging and spectral artefacts via product–structure correlation.

Data availability

The raw data and videos that support the findings of this study are publicly available through the AC/CATLAB Archive (https://ac.archive.fhi.mpg.de/D60951) or from the corresponding authors. Source data are provided with this paper.

References

1. Schlögl, R. Heterogeneous catalysis. *Angew. Chem. Int. Ed.* **54**, 3465–3520 (2015).
2. Greiner, M. T., Jones, T. E., Klyushin, A., Knop-Gericke, A. & Schlögl, R. Ethylene epoxidation at the phase transition of copper oxides. *J. Am. Chem. Soc.* **139**, 11825–11832 (2017).
3. Prigogine, I. & Nicolis, G. in *Bifurcation Analysis: Principles, Applications and Synthesis* (eds Hazewinkel, M., Jurkovich, R. & Paelinck, J. H. P.) 3–12 (Springer, 1985).
4. Imbihl, R. & Ertl, G. Oscillatory kinetics in heterogeneous catalysis. *Chem. Rev.* **95**, 697–733 (1995).
5. Greiner, M. T. et al. Phase coexistence of multiple copper oxides on AgCu catalysts during ethylene epoxidation. *ACS Catal.* **8**, 2286–2295 (2018).
6. Nettesheim, S., von Oertzen, A., Rotermund, H. H. & Ertl, G. Reaction diffusion patterns in the catalytic CO-oxidation on Pt(110): front propagation and spiral waves. *J. Chem. Phys.* **98**, 9977–9985 (1993).
7. Ertl, G. Molecules at surfaces: 100 years of physical chemistry in Berlin-Dahlem. *Angew. Chem. Int. Ed.* **52**, 52–60 (2013).
8. Ertl, G. Reactions at surfaces: from atoms to complexity (Nobel Lecture). *Angew. Chem. Int. Ed.* **47**, 3524–3535 (2008).
9. Schaak, A. & Imbihl, R. Bistability and formation of low work function areas in the O_2+H_2 reaction on a Rh(111) surface. *J. Chem. Phys.* **113**, 9822–9829 (2000).
10. Barroo, C., De Decker, Y., Visart de Bocarmé, T. & Kruse, N. Complex oscillation patterns during the catalytic hydrogenation of NO_2 over platinum nanosized. *Cryst. J. Phys. Chem. C* **118**, 6839–6846 (2014).
11. Kaichev, V. V. et al. Evolution of self-sustained kinetic oscillations in the catalytic oxidation of propane over a nickel foil. *J. Catal.* **334**, 23–33 (2016).
12. Hendriksen, B. L. M., Bobaru, S. C. & Frenken, J. W. M. Bistability and oscillations in CO oxidation studied with scanning tunnelling microscopy inside a reactor. *Catal. Today* **105**, 234–243 (2005).
13. Gladky, A. Y., Kaichev, V. V., Ermolaev, V. K., Bukhtiyarov, V. I. & Parmon, V. N. Propane oxidation on nickel in a self-oscillation mode. *Kinet. Catal.* **46**, 251–259 (2005).
14. Bychkov, V. Y., Tyulenin, Y. P., Slinko, M. M. & Korchak, V. N. Autonomous and forced oscillations during methane oxidation over cobalt catalysts. *Appl. Catal. A* **321**, 180–189 (2007).
15. Sales, B. C., Turner, J. E. & Maple, M. B. Oscillatory oxidation of CO over Pt, Pd and Ir catalysts: Theory. *Surf. Sci.* **114**, 381–394 (1982).
16. Ertl, G., Norton, P. R. & Rüstig, J. Kinetic oscillations in the platinum-catalyzed oxidation of Co. *Phys. Rev. Lett.* **49**, 177–180 (1982).
17. Cao, J. et al. In situ observation of oscillatory redox dynamics of copper. *Nat. Commun.* **11**, 3554 (2020).
18. Bychkov, V. Y., Tyulenin, Y. P., Slinko, M. M. & Korchak, V. N. Oscillatory behaviour during C_2–C_4 hydrocarbon oxidation over palladium catalysts. *Catal. Lett.* **141**, 602–607 (2011).
19. Bychkov, V. Y., Tyulenin, Y. P., Slinko, M. M. & Korchak, V. N. Oscillatory behaviour during ethane oxidation over nickel and cobalt catalysts. *Catal. Lett.* **119**, 339–345 (2007).
20. Deng, Y. & Nevell, T. G. Oscillations of methane combustion over alumina-supported palladium catalysts under oxygen-deficient conditions. *J. Mol. Catal. A* **142**, 51–60 (1999).
21. Tang, X., Nan, Y., Huang, F. & Zhang, X. Oscillations of methane oxidation over metallic nickel surfaces. *React. Kinet. Mech. Catal.* **107**, 245–252 (2012).
22. Tulenin, Y. P., Sinev, M. Y., Savkin, V. V. & Korchak, V. N. Dynamic behaviour of Ni-containing catalysts during partial oxidation of methane to synthesis gas. *Catal. Today* **91-92**, 155–159 (2004).

23. Saraev, A. A. et al. The origin of self-sustained reaction-rate oscillations in the oxidation of methane over nickel: an operando XRD and mass spectrometry study. *Catal. Sci. Technol.* **7**, 1646–1649 (2017).

24. Flytzani-Stephanopoulos, M., Schmidt, L. D. & Caretta, R. Steady state and transient oscillations in NH_3 oxidation on Pt. *J. Catal.* **64**, 346–355 (1980).

25. Pyatnitskii, Y. I. & Filonenko, G. V. On the mechanism of auto-oscillations in CO hydrogenation on supported palladium catalysts. *React. Kinet. Catal. Lett.* **44**, 499–503 (1991).

26. Xiang, Y., Kovarik, L. & Kruse, N. Rate and selectivity hysteresis during the carbon monoxide hydrogenation over promoted Co/MnOx catalysts. *Nat. Commun.* **10**, 3953 (2019).

27. Khrustova, N., Veser, G., Mikhailov, A. & Imbihl, R. Delay-induced chaos in catalytic surface reactions: NO reduction on Pt(100). *Phys. Rev. Lett.* **75**, 3564–3567 (1995).

28. Schroder, U. Kinetic oscillations during acetylene hydrogenation over Pt/Al₂O₃ and Pd/Al₂O₃ in the presence of CO. *J. Catal.* **146**, 586–590 (1994).

29. Petrov, L. et al. Thermal oscillations during the catalytic hydrogenation of nitrobenzene. *J. Mol. Catal.* **54**, 237–242 (1989).

30. Helveg, S. et al. Observing gas-catalyst dynamics at atomic resolution and single-atom sensitivity. *Micron* **68**, 176–185 (2015).

31. Lavoie, J.-M. Review on dry reforming of methane, a potentially more environmentally-friendly approach to the increasing natural gas exploitation. *Front. Chem.* **2**, 1–17 (2014).

32. Wittich, K., Krämer, M., Bottke, N. & Schunk, S. A. Catalytic dry reforming of methane: insights from model systems. *ChemCatChem* **12**, 2130–2147 (2020).

33. Sandoval-Diaz, L. E., Schlögl, R. & Lunkenbein, T. Quo vadis dry reforming of methane? —A review on its chemical, environmental, and industrial prospects. *Catalysts* **12**, 465 (2022).

34. Sandoval-Diaz, L. et al. Visualizing the importance of oxide-metal phase transitions in the production of synthesis gas over Ni catalysts. *J. Energy Chem.* **50**, 178–186 (2020).

35. Wang, Z.-J. et al. Direct observation of graphene growth and associated copper substrate dynamics by in situ scanning electron microscopy. *ACS Nano* **9**, 1506–1519 (2015).

36. Jin, Y. et al. Image matching across wide baselines: from paper to practice. *Int. J. Comput. Vis.* **129**, 517–547 (2021).

37. Carley, A. F., Jackson, S. D., O'Shea, J. N. & Roberts, M. W. The formation and characterisation of Ni^{3+}—an X-ray photoelectron spectroscopic investigation of potassium-doped Ni(110)–O. *Surf. Sci.* **440**, L868–L874 (1999).

38. Kaichev, V. V. et al. In situ XPS study of self-sustained oscillations in catalytic oxidation of propane over nickel. *Surf. Sci.* **609**, 113–118 (2013).

39. Uhlenbrock, S., Scharfschwerdt, C., Neumann, M., Illing, G. & Freund, H. J. The influence of defects on the Ni 2p and O 1s XPS of NiO. *J. Phys. Condens. Matter* **4**, 7973–7978 (1992).

40. Wang, H.-Y. et al. Direct evidence of subsurface oxygen formation in oxide-derived Cu by X-ray photoelectron spectroscopy. *Angew. Chem. Int. Ed.* **61**, e202111021 (2022).

41. Weger, L., Abánades, A. & Butler, T. Methane cracking as a bridge technology to the hydrogen economy. *Int. J. Hydrog. Energy* **42**, 720–731 (2017).

42. Alstrup, I., Chorkendorff, I. & Ullmann, S. Dissociative chemisorption of CH_4 on Ni(100) with preadsorbed oxygen. *Surf. Sci.* **234**, 79–86 (1990).

43. Blanksby, S. J. & Ellison, G. B. Bond dissociation energies of organic molecules. *Acc. Chem. Res.* **36**, 255–263 (2003).

44. Wei, J. & Iglesia, E. Reaction pathways and site requirements for the activation and chemical conversion of methane on Ru-based catalysts. *J. Phys. Chem. B* **108**, 7253–7262 (2004).

45. Bossche, M. V. D. & Grönbeck, H. Methane oxidation over PdO(101) revealed by first-principles kinetic modeling. *J. Am. Chem. Soc.* **137**, 12035–12044 (2015).

46. Vogt, C. et al. Understanding carbon dioxide activation and carbon–carbon coupling over nickel. *Nat. Commun.* **10**, 5330 (2019).

47. Xu, J. & Froment, G. F. Methane steam reforming, methanation and water-gas shift: I. Intrinsic kinetics. *AIChE J.* **35**, 88–96 (1989).

48. Park, J.-W. & Altstetter, C. J. The diffusion and solubility of oxygen in solid nickel. *Metall. Trans. A* **18**, 43–50 (1987).

49. Garruchet, S., Politano, O., Arnoux, P. & Vignal, V. Diffusion of oxygen in nickel: a variable charge molecular dynamics study. *Solid State Commun.* **150**, 439–442 (2010).

50. Couper, J. R., Penney, W. R., Fair, J. R., Walas, S. M. in *Chemical Process Equipment (Revised Second Edition)* (eds Couper, J. R., Penney, W. R., Fair, J. R. & Walas, S. M.) 553–580 (Gulf Professional Publishing, 2010).

51. Kharatyan, S. L., Chatilyan, H. A. & Manukyan, K. V. Kinetics and mechanism of nickel oxide reduction by methane. *J. Phys. Chem. C* **123**, 21513–21521 (2019).

52. Hendriksen, B. L. M. et al. The role of steps in surface catalysis and reaction oscillations. *Nat. Chem.* **2**, 730–734 (2010).

53. Lashina, E. A., Vinokurov, Z. S., Saraev, A. A. & Kaichev, V. V. Self-sustained oscillations in oxidation of methane over palladium: experimental study and mathematical modeling. *J. Chem. Phys.* **157**, 044703 (2022).

54. Zhang, X., Lee, C. S. M., Hayward, D. O. & Mingos, D. M. P. Oscillatory behaviour observed in the rate of oxidation of methane over metal catalysts. *Catal. Today* **105**, 283–294 (2005).

55. Zhang, X., Lee, C. S. M., Mingos, D. M. P. & Hayward, D. O. Oscillatory behaviour during the partial oxidation of methane over cobalt wires and foils. *Appl. Catal. A* **248**, 129–142 (2003).

56. Zhang, X., Lee, C. S. M., Mingos, D. M. P. & Hayward, D. O. Oscillatory behaviour during the oxidation of methane over palladium metal catalysts. *Appl. Catal. A* **240**, 183–197 (2003).

57. Wood, B. R., Reimer, J. A., Bell, A. T., Janicke, M. T. & Ott, K. C. Methanol formation on Fe/Al-MFI via the oxidation of methane by nitrous oxide. *J. Catal.* **225**, 300–306 (2004).

58. Tabor, E. et al. Low-temperature selective oxidation of methane over distant binuclear cationic centers in zeolites. *Commun. Chem.* **2**, 71 (2019).

59. Schindelin, J. et al. Fiji: an open-source platform for biological-image analysis. *Nat. Methods* **9**, 676–682 (2012).

60. Lee, G. R., Gommers, R., Waselewski, F., Wohlfahrt, K. & O'Leary, A. PyWavelets: a Python package for wavelet analysis. *J. Open Source Softw.* **4**, 1237 (2019).

61. Sawhney, K. J. S. et al. A novel undulator-based PGM beamline for circularly polarised synchrotron radiation at BESSY II. *Nucl. Instrum. Methods Phys. Res. A* **390**, 395–402 (1997).

62. Knop-Gericke, A. et al. in *Advances in Catalysis* 52 (eds Gates, B. C., Knözinger, H., Jentoft, F. C.) 213–272 (Academic Press, 2009).

63. Salmeron, M. & Schlögl, R. Ambient pressure photoelectron spectroscopy: a new tool for surface science and nanotechnology. *Surf. Sci. Rep.* **63**, 169–199 (2008).

Acknowledgements

Author contributions

L.S.-D. and D.I. constructed the operando ESEM quartz reactor. L.S.-D. carried out the operando ESEM experiments. L.S.-D., D.C., T.G. and M.H. carried out the NAP-XPS experiments. A.H. prepared the catalyst cross-section by FIB. M.P. analysed the cross-section sample by TEM imaging. M.V., G.D. and C.S. contributed to computer vision analysis and discussion of the videos. L.S.-D., D.C, M.V. and T.L. analysed the operando spectromicroscopy and post-reaction data. L.S.-D. and T.L. wrote the manuscript. T.L., R.S. and A.K.-G. conceived the project. T.L., R.S., C.S., K.R. and A.K.-G. guided the research. All authors discussed the results and commented on the manuscript.

Competing interests

The authors declare no competing interests.

Additional information

Supplementary information The online version contains supplementary material available at https://doi.org/10.1038/s41929-023-01090-4.

Correspondence and requests for materials should be addressed to Luis Sandoval-Diaz or Thomas Lunkenbein.

Peer review information *Nature Catalysis* thanks Vasily V. Kaichev and the other, anonymous, reviewer(s) for their contribution to the peer review of this work.

Reprints and permissions information is available at www.nature.com/reprints.

Publisher's note Springer Nature remains neutral with regard to jurisdictional claims in published maps and institutional affiliations.